Stability and catalytic properties of nanostructured carbons in electrochemical environments

S. Pérez-Rodríguez[a,1], D. Sebastián[a], M.J. Lázaro[a*], E. Pastor[b*]

[a]Instituto de Carboquímica (CSIC), Miguel Luesma Castán 4, 50018 Zaragoza, Spain.

[b]Universidad de La Laguna, Dpto. Química-Física, Avda. Astrofísico Francisco Sánchez s/n, 38071 La Laguna (Tenerife), Spain.

[1]Present address: Centre Tecnològic de la Química de Catalunya (CTQC) Marcel·lí Domingo s/n, 43007 Tarragona, Spain.

* Corresponding author:

M.J. Lázaro: Tel.: +34 976733977; Fax: +34 976733318; E-mail address: mlazaro@icb.csic.es

E. Pastor: Tel.: +34 92231 8071; Fax: +34 922318002; E-mail address: epastor@ull.es.

Abstract

This work reports a study of the electrocatalytic properties and stability of nanostructured carbon electrodes by on-line differential electrochemical mass spectrometry (DEMS). A wide electrochemical characterization in 0.1 M $NaHCO_3$ involving anodic (carbon corrosion and oxygen evolution reaction, OER) and cathodic (CO_2 reduction and hydrogen evolution reaction, HER) key reactions in energy-conversion devices was performed. DEMS studies showed that the faradaic current from 1.3 to 1.6 V vs. RHE of carbons was only associated to CO_2 formation by corrosion and not to OER, the stability being improved by the graphitic character of carbon. H_2 evolution was also enhanced with graphitic carbon nanofilaments, even though metal traces might positively influence their catalytic activity. By comparison of the faradaic currents and the H_2 formation signals, in the absence and presence of CO_2, a high inhibition of the HER was established for all carbon electrodes due to the species adsorption from CO_2 reduction.

Keywords: Nanostructured carbons, DEMS, corrosion, O_2 evolution, H_2 evolution, CO_2 electroreduction.

1. Introduction

Noble metals or metal oxides supported on carbon materials are conventionally used as catalysts in renewable energy conversion and storage devices, for example in polymer electrolyte membrane (PEM) fuel cells and metal-air batteries [1-7].

The commercial carbon black Vulcan XC-72R (supplied by Cabot) is the most commonly used material in the field of electrocatalysis because of their adequate mesoporous distribution and good electrical properties [4, 8]. However, much research effort has been made using advanced nanostructured carbon materials (NCMs) over the last decades, such as graphenes [1], carbon nanotubes (CNTs) [3, 9, 10], carbon nanofibers (CNFs) [3, 11], carbon nanocoils (CNCs) [12, 13], carbon xerogels (CXs) [14, 15], carbon nanocages [5] and ordered mesoporous carbons (OMCs) [2]. These materials offer optimal textural and chemical features which lead to an enhanced performance. For example, OMCs and CXs provide a high surface area and a developed mesoporosity which is essential for achieving a good dispersion of metal nanoparticles and to favour the diffusion of reactants and by-products. Another key specification is the stability of the carbon material since carbon-support corrosion is considered to be one of the main problems facing the performance of fuel cells [16-20]. Also, a high electrical conductivity is required to facilitate electron transfer [3, 4, 14]. In order to solve these issues, more graphitic carbons (e.g., CNTs and CNFs) have been used [3, 9, 10].

Carbon-supported catalysts have been also used in the electrochemical reduction of CO_2 obtaining promising results [21-25]. An enhanced activity was reached on these carbon-based electrocatalysts in comparison to massive metal electrodes, which may be explained by a better distribution of CO_2 on the active surface. However, few efforts have been made involving advanced NCMs [26-28].

On the other hand, the use of carbon electrodes for electrochemical energy conversion and storage applications has received special attention during the last years [6, 24, 29-37]. In this context, Zhang and coworkers [6] obtained good electrocatalytic properties for both oxygen reduction and evolution reactions on a N,P-doped mesoporous carbon foam. On the other hand, Wu et al. [36] reported high Faradaic efficiencies (up to 90%) for CO_2 reduction to ethylene and ethanol on nanometre-size N-doped graphene quantum dots. Finally, the hydrogen evolution reaction (HER) has been also recently studied on carbon electrodes obtaining promising results [32, 37].

The electrochemical behaviour of carbon materials for energy-conversion applications has been evaluated in detail using conventional electrochemical techniques, as cyclic voltammetry or chronoamperometry [1, 8, 20, 37-42]. However, these measurements do not allow distinguishing between the current signals associated with the production of different species at the electrode surface in the same potential region. For example, oxygen evolution reaction (OER) by water oxidation takes place at potentials above 1.23 V vs. RHE, and consequently, it is accompanied by carbon corrosion. In contrast, the hydrogen formation is a competitive reaction, which occurs during the CO_2 reduction in aqueous electrolytes. This limitation can be resolved by using differential electrochemical mass spectrometry (DEMS), coupling on-line an electrochemical cell to a mass spectrometer. In this way, DEMS allows simultaneously following the electrochemical properties of electrodes and the volatile and gaseous species generated on the electroactive surface, with excellent sensitivity and under potential control. Therefore, DEMS is a powerful in situ tool to investigate the electrochemical behaviour of carbon materials and to elucidate the reaction pathways taking place [16, 17, 21, 43, 44]. But this technique is not commercial and the DEMS configuration has to be adapted for every application.

In this work, the electrochemical stability and catalytic behaviour of various nanostructured carbons has been established by DEMS. In particular, OMCs, two types of graphitic carbons, CNFs and CNCs, and the commercial carbon black Vulcan XC-72R, have been used. Different cathodic and anodic electrochemical processes have been studied: capacitive properties, tolerance to corrosion and activity toward HER and OER. Furthermore, carbons have been tested in the electrochemical reduction of CO_2. To the best of our knowledge, it is the first work reporting an extensive study of the electrochemical properties and stability of different nanostructured carbons by in-situ electrochemical mass spectrometry.

2. Experimental

2.1 Synthesis of nanostructured carbon materials

OMCs were prepared by the nanocasting technique using a mesoporous silica (SBA-15) as template and a furan resin/acetone as carbon precursor. Finally, OMCs were washed with 1.1 M NaOH in order to remove the silica particles [22, 45].

CNFs were synthesized by methane decomposition at 700 ºC over a $NiCuAl_2O_3$ (atomic ratio 78:6:16) catalyst. After CNF synthesis, the metal particles were removed by means of an oxidation treatment with concentrated nitric acid (65 wt%, Panreac) at room temperature for 2 h [11, 22].

CNCs were prepared by the catalytic graphitization method using Ni and Co nitrates as graphitization catalysts, a mixture of resorcinol and formaldehyde as the carbon precursor and silica sol to generate mesoporosity. Obtained CNCs were first washed with 1.1 M NaOH (98 wt%, Panreac) solution to remove the silica particles, and subsequently treated with concentrated nitric acid (65 wt%, Panreac) at room temperature for 2 h for eliminating the metal content [22, 46].

In addition to the removal of metal nanoparticles, the treatment with nitric acid led to the creation of a low concentration of oxygen functionalities on CNFs and CNCs, especially carbonyl/quinone groups (see Supporting Information; Tables S1 and S2). The treatment at low temperature was selected to preserve the original structure of nanofibers and nanocoils while removing the non-encapsulated metal [46-48].

2.2 Physicochemical characterization

Transmission electron microscopy (TEM) micrographs of the NCMs were obtained using a JEOL-2000 FXII microscope equipped with a LaB6 gun at 200 kV and with a spatial resolution of 0.28 nm. To obtain the micrographs, the samples were finely grinded and ultrasonically dispersed in ethanol. A drop of the resultant dispersion was deposited and dried onto a standard copper grid coated with Lacey carbon.

X-ray diffraction (XRD) patterns of the materials were recorded using a Bruker AXS D8 Advance diffractometer with a θ–θ configuration and with Cu Kα radiation.

N_2 adsorption-desorption isotherms of the NCMs were measured at -196 ºC using a Micromeritics ASAP 2020. The total surface area was calculated from BET (Brunauer, Emmett and Teller) equation and the total pore volume was determined using the single point method at $P/P_0 = 0.99$. V_{meso} and average pore sizes (D_p) were obtained from the analysis of the desorption branch of the N_2 isotherm using the BJH (Barrett, Joyner and Halenda) method.

Thermogravimetric analyses (TGA) were carried out on a thermogravimetric SETARAM Setsys Evolution under air atmosphere. The temperature was varied between room temperature and 950 ºC with a heating rate of 5 ºC min^{-1}.

Temperature programmed desorption (TPD) experiments were carried out in an AutoChem II 2920 apparatus to determinate the amount of surface oxygen groups on carbon materials. The profiles of desorbed CO and CO_2 were obtained in a quartz

144 reactor heated under a constant flow of Ar (50 $mLmin^{-1}$) at a heating rate of 10 ºCmin^{-1}
145 up to 1000 ºC. The amounts of CO and CO_2 desorbed from the carbon samples were
146 analyzed online by mass spectroscopy. The total amount of CO and CO_2 released was
147 calculated by integrating the area under the flow rate versus time curve. Furthermore,
148 the ratio CO/CO_2 was obtained as a measure of the surface acidity. The deconvolution
149 of TPD profiles was performed using a multiple Gaussian function and a non-linear
150 least-squared optimization procedure based on the Levenberg-Marquardt algorithm
151 using the software Fytik and assigning as initial estimate distinct desorption
152 temperatures for each group [49, 50]. The CO and CO_2 evolution and the deconvoluted
153 TPD profiles are shown in the Supporting Information (see Figures S1 and S2).
154 X-ray photoelectron spectroscopy (XPS) analyses were carried out with an
155 ESCAPlus OMICRON system equipped with a hemispherical electron energy analyser.
156 The spectrometer operated at 150 W (15 mA, 10 kV), using a non-monochromatized
157 MgKα (1253.6 eV) anode and under vacuum ($<5 \cdot 10^{-9}$) over an area of sample of
158 1.75×2.75 mm. A survey scan (1sweep/200 ms dwell) was acquired between 0 and 1100
159 eV, at 0.5 eV step, 0.2 s dwell and 50 eV pass energy. Detailed scans for C 1s and O 1s
160 were obtained at 0.1 eV step, 0.5 s dwell and 20 eV pass energy. For calibration
161 purposes, the C 1s binding energy of the graphitic peak (BE) was referenced at 284.6
162 eV. C and O content was calculated from the corresponding peak areas divided by the
163 appropriate sensitive factors (1.00 for C 1s and 2.85 for O 1s) using the CASAXPS
164 software after Shirley background subtraction. Figure S3 shows the survey XPS spectra
165 and C1s and O1s regions for a selected sample: Vulcan XC-72R.
166 Elemental analysis (EA) of carbon materials were performed in a CHNS-O
167 Analyzer Thermo FlashEA 1112.

Inductively coupled plasma atomic emission spectroscopy (ICP-AES) were performed on a Jobin Ybon 2000 spectrometer to determine the silica and metal residues in the carbon matrixes (Table S3).

2.3. Electrochemical and spectro-electrochemical characterization

Spectro-electrochemical measurements were carried out at room temperature and atmospheric pressure in a three electrodes electrochemical cell directly attached to a mass spectrometer (Balzers Omnistar quadrupole mass spectrometer), with a Faraday cup detector. The potentiostat-galvanostat was an Autolab PGSTAT302 (Ecochemie). Further details about DEMS set-up can be found elsewhere [51]. A high surface area carbon rod was used as counter electrode, whereas an Ag/AgCl/3M KCl electrode (0.21 V vs. normal hydrogen electrode, NHE) placed inside a Luggin capillary was employed as reference. Unless otherwise specified, all potentials in the text are referred to the reversible hydrogen electrode (RHE). The working electrode was prepared depositing a thin-layer of the corresponding carbon over a glassy carbon (GC) susbtrate (7.0 mm of diameter, SIGRADUR® G). Carbon suspensions were prepared by mixing 2 mg of the sample, 15 μL of Nafion dispersion (5 wt%, Aldrich) and 500 μL of ultrapure water (Millipore Milli-Q system). The suspension was sonicated for 90 min before deposition. The Nafion content of the carbon thin-film was selected on the basis of previous works for a convenient attachment of NCMs to the electrode surface, but not leading to extensive surface blocking [52]. The capacitance of nanocarbon materials was calculated from the charge in the region 0.3-0.8 V vs. RHE in the base electrolyte by considering the averaged value from positive and negative going scans of cyclic voltammetry performed from -0.1 to 1.6 V vs. RHE.

DEMS experiments were carried out in a 0.1 M $NaHCO_3$ (Merck, p.a.) electrolyte solution deaerated with Ar (pH = 8.4). An aliquot of 10 µL of the carbon ink was deposited onto the carbon disk and dried to room temperature before every electrochemical characterization, each performed with different potential windows. Freshly prepared working electrodes were used for the capacitance properties and corrosion behaviour on one hand, and the hydrogen evolution and CO_2 reduction on the other hand. For the latter, CO_2 (99.99 %, Air Liquide) was bubbled into the electrolyte for 30 min in order to obtain a CO_2 saturated 0.1 M $NaHCO_3$ solution (pH = 6.8) and the performance of carbons for CO_2 reduction was established.

3. Results

3.1 Physicochemical characterization of nanostructured carbon materials

The morphology of NCMs was studied by TEM (see Figure 1a-d). Vulcan is formed by an aggregation of spherical carbon nanoparticles composed of small crystallites. OMCs present an ordered structure, which consists of amorphous carbon nanorods with uniform mesopores. Finally, CNFs and CNCs show well-aligned graphitic layers, forming carbon nanofilaments with "fishbone" morphology or curved ribbons, respectively.

The crystalline structure of carbon materials was analysed by XRD. The diffraction patterns have been previously published and can be consulted elsewhere [22]. All the samples, with the exception of OMCs, showed a peak around $2\theta = 25^{\circ}$, which is associated with the graphite (002) diffraction. The relative intensity of the (002) peak, and hence, the graphitization degree of the carbons, increased in the order: Vulcan < CNCs < CNFs. Finally, OMCs did not show diffraction at $2\theta = 25^{\circ}$ due to the amorphous nature of carbon.

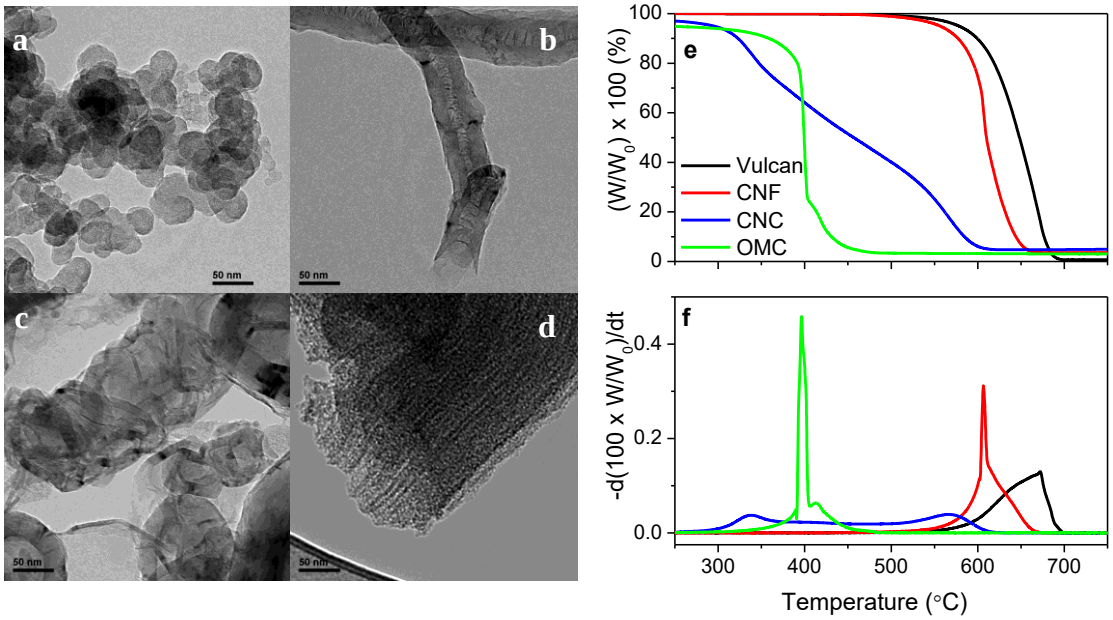

Figure 1. TEM images of (a) Vulcan, (b) CNF, (c) CNC and (d) OMC. TG profiles in air of carbon materials in terms of (e) weight percentage and (f) mass variation velocity as a function of the temperature.

Structural information of NCMs was deduced from TGA in air. Figure 1e shows the TG profiles for all the carbon materials, while Figure 1f displays the rate of mass loss. Different TG profiles were found for the NCMs. OMCs and CNFs presented a pronounced mass loss around 400 and 600ºC, respectively, which is associated with carbon combustion. OMCs displayed less oxidation tolerance due to their amorphous character, while graphitic CNFs showed an improved condition toward combustion. In contrast, two broad oxidation peaks centred at 338 and 567 ºC were obtained in the derivative curve vs. temperature (Figure 1f) for CNCs, indicating the presence of two kinds of carbon phases with different nature: the first peak can be ascribed to the oxidation of the amorphous phase, while the second one can be attributed to the graphitic fraction. Finally, Vulcan presented the highest oxidation resistance with a

gasification temperature at 672 ºC. Other authors have obtained similar results [53-56]. As general trend, the oxidation temperature is higher as the carbon crystallinity increases. Indeed, the synthetic materials follow this sequence. However, a lower thermal stability would be expected for Vulcan. This behaviour could be explained by the presence of sulphur groups (0.62 wt% from EA) which can increase the oxidation resistance [57, 58]. Additionally, despite the low residual metal content of CNCs and CNFs (below 1 wt% according to the results obtained by ICP (Table S3), it may act as an oxidation catalyst, decreasing the onset temperature for the burn-off of these carbons [47].

Textural properties of the NCMs were studied by N_2-physisorption and the results are summarized in Table 1. OMCs present the highest adsorption capacity whereas CNFs display the lowest surface area although with a significant mesoporosity (98% in terms of pore volume). On the other hand, the commercial carbon and CNCs show similar surface areas and mesopore contribution. Regarding the average pore size, Vulcan and CNFs exhibit larger pores (10-11 nm) than OMCs and CNCs (4 nm).

Table 1. Textural parameters of carbon materials: total BET surface area (S_{BET}), total pore volume (V_T), mesopore volume (V_{meso}), mesopore fraction (in terms of pore volume) and average pore diameter (D_p).

Sample	S_{BET} ($m^2\ g^{-1}$)	V_T ($cm^3\ g^{-1}$)	V_{meso} ($cm^3\ g^{-1}$)	Mesopore fraction (%)	D_p (nm)
Vulcan	238	0.38	0.31	83	10.4
CNF	76	0.24	0.24	98	11.5
CNC	234	0.17	0.13	78	4.1
OMC	812	0.55	0.31	57	3.8

TPD experiments provided a good insight on surface oxygen group distribution of the NCMs. Table 2 shows the amounts of CO and CO_2 released, obtained by the integration of the areas under the TPD peaks versus time, together with the oxygen content (O_{TPD}, wt%). The number of oxygen atoms per surface area is also presented, considering the S_{BET} obtained on the N_2 physisorption experiments (Table 1). Interestingly, CNCs and CNFs present high oxygen contents per surface area (11.0 and 3.7 atoms nm^{-2}, respectively) due to the creation of functional groups during the metal removing treatment with nitric acid (see Supporting Information, Tables S1 and S2). Although CNFs and CNCs were subjected to the same purification treatment, the oxygen content for the former material was much lower (~3 times in terms of O atoms nm^{-2}). In this context, CNFs present a low amount of defects due to their highly graphitic character, leading to a low reactivity for the creation of oxygenated species.

The oxygen content was also determined by means of elemental analysis (EA) (Table 2, O_{EA}). This technique provides an oxygen content closer to the amount in the samples considered as a bulk material. Results correlated quite well with the TPD measurements, showing that the volatile matter of these samples corresponds with the amounts of CO and CO_2 desorbed. However, an O_{TPD} amount of 4.8 wt% was obtained on OMCs, while around 2 times more (8.4 wt%) was measured from EA. This behaviour may be explained by surface groups in interior sites which are not desorbed at 1000 ºC due to diffusion restrictions caused by the low pore size (4 nm) and the high surface area (812 m^2g^{-1}) of this material. TPD allows determining only oxygen groups that are desorbed during temperature variation, *i.e.* available for desorption [59], while EA considers the whole sample. This means that almost half of oxygen groups present in OMC are occluded in small or even blind/closed pores and did not desorb at temperatures below 1000ºC.

Finally, XPS was also used as a complementary method to obtain the surface oxygen content (Table 2, O_{XPS}). Higher oxygen contents were determined by XPS for all the materials in comparison to those obtained by TPD or EA. XPS is a surface sensitive technique which accounts only for the elements a few nanometers close to the analysis surface. In our case, carbon atoms in the bulk do not contribute to the XPS signal. Thus, the general trend concerning higher O_{XPS} values compared to O_{TPD} and/or O_{EA} indicates that oxygen functional groups are mainly present on the surface of carbons and not in the carbon matrix, as expected.

The nature and the amount of surface oxygen functional groups were estimated from deconvolution of TPD profiles. Acidic groups (carboxylic and lactones) are decomposed into CO_2 at lower temperatures, whereas basic and neutral groups (phenols, quinones and carbonyls) are desorbed as CO at higher temperatures. Anhydrides originate both CO_2 and CO [49]. Table 3 summarizes the estimated distribution of oxygen functional groups obtained from the deconvolution of CO and CO_2 evolutions.

Table 2. Surface chemistry measured by TPD (total amount of CO and CO_2 released, CO/CO_2 ratio and total oxygen content), XPS (surface oxygen content) and EA (total oxygen content) of carbon materials. The number of oxygen atoms per surface area was obtained considering the total O_{TPD} and the S_{BET} from N_2 physisorption isotherms.

Sample	CO ($\mu mol\ g^{-1}$)	CO_2 ($\mu mol\ g^{-1}$)	CO/CO_2	O_{TPD} (wt%)	O ($atoms\ nm^{-2}$)	O_{EA} (wt%)	O_{XPS} (wt%)
Vulcan	174	106	1.7	0.6	1.0	0.4	2.3
CNF	320	71	4.5	0.7	3.7	1.2	4.7
CNC	2602	832	3.1	6.8	11.0	6.8	9.3
OMC	1475	770	1.9	4.8	2.2	8.4	11.1

Table 3. Results from deconvolution of CO_2 and CO TPD profiles of carbon materials (mol %). Carboxylic acids were obtained by the sum of the amounts obtained from peaks 1 and 2 of the CO_2 profiles.

Sample	Carboxylic acid	Anhydride	Lactone	CO desorption	Phenol	Carbonyl/ Quinone
Vulcan	37	6	19	11	5	24
CNF	10	11	9	15	13	43
CNC	18	10	1	12	24	36
OMC	27	15	4	11	21	23

A different oxygen functional group distribution was found for the NCMs. Phenol and carbonyl/quinone groups were predominant for the materials subjected to the purification treatment with nitric acid. These groups are generated during the oxidation treatment with nitric acid, as it is shown in Supporting Information (Tables S1 and S2). In contrast, a large contribution of acid groups (carboxylic acids and lactones) was developed for Vulcan and OMCs. In agreement with these results, a lower value of the ratio CO/CO_2 (see Table 2) was obtained for the last materials (around 2). In contrast, CNFs and CNCs presented high ratios (4.5 and 3.1, respectively), indicating an enhanced surface basicity as a result of the purification treatment with HNO_3 [60].

3.2 Electrochemical and spectro-electrochemical characterization

3.2.1 Capacitance properties

Cyclic voltammograms (CVs) were recorded at 5 and 50 mV s^{-1} in 0.1 M $NaHCO_3$ cycling the potential between -0.1 and 1.6 V vs. RHE. The specific capacitance, *C*, was calculated from the correlation between current density, *i*, and the variation of potential, E, with time, t, by using the Equation 1:

$$i\ [A\ g^{-1}] = C\ [F\ g^{-1}] \cdot dE(V)/dt(s) \quad (1)$$

where *dE/dt* is the scan rate, being constant in our experiments. The curves of specific capacitance versus potential are given in Figure 2.

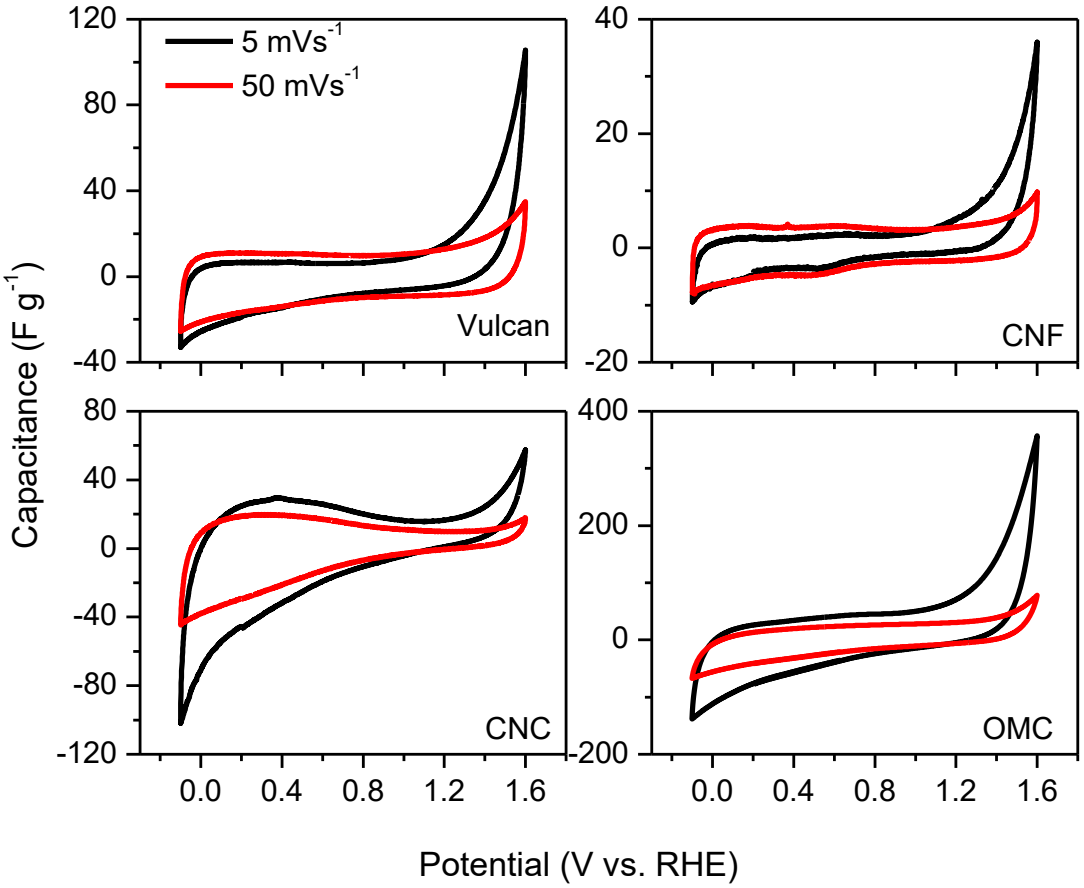

Fig. 2. CVs of carbon materials in 0.1 M $NaHCO_3$.

All carbon materials displayed a double-layer capacitive behaviour [61] together with anodic current rapidly increasing with high positive potential starting at about 1 V vs. RHE. The latter is associated to irreversible reaction (carbon oxidation as will be discussed in following sections) as indicated by differences between the two scan rates reported (5 and 50 mV s^{-1}). However, different profiles are evident from comparison of the double layer currents and the behaviour at potentials approaching 0 V vs. RHE. Capacitance values are summarized in Table 4, calculated from the averaged value in the interval 0.3-0.8 V vs. RHE, where no carbon oxidation occurs. OMCs showed the

highest capacitance owing to their large specific surface area (812 m^2 g^{-1}), while CNFs presented the lowest value in correlation with the low BET surface area of this carbon (76 m^2 g^{-1}). Indeed, the capacitance (Table 4, F g^{-1}) approximately follows the trend of BET surface area (Table 1, m^2 g^{-1}). Furthermore, the graphitic character of CNFs influences also the values of capacitance as charges are preferably accumulated on the defects [61, 62]. In addition, a small pseudocapacitance contribution was observed on CNCs and CNFs (0.4-0.7 V vs. RHE) associated with the reversible oxidation/reduction of quinone groups generated during the oxidation treatment of the samples with nitric acid [63], as was determined by TPD. This contribution was lower for CNFs due to the smaller amount of oxygen per surface area. Interestingly, CNCs exhibited a dramatic decrease of capacitance from about 0.5 V to 1.4 V vs. RHE, which may be related to the porosity saturation as pointed out by Mysyk et al. [64]. They reported a decrease of the double-layer current as a consequence of a porous volume not sufficiently developed, as correlated to nitrogen physisorption ex-situ measurements.

In contrast, Vulcan and OMCs did not present pseudocapacitance as a higher contribution of acid groups (e.g. carboxylic acids and lactones), which are electrochemically inactive in the double layer region [65], was obtained for these materials (Table 3). OMCs showed higher ohmic resistance than the other NCMs, as envisaged from the positive slope of capacitance vs. potential, due to its amorphous character, leading to a low electrical conductivity.

Table 4. Electrochemical features of nanocarbon materials. Normalized ionic currents are referred to the m/z = 44, ascribed to CO_2 evolution.

Sample	Capacitance ($F\ g^{-1}$)	Faradaic current at 1.5 V vs. RHE ($A\ g^{-1}$)	Ionic current (m/z = 44) at 1.5 V vs. RHE ($mA\ bar^{-1}$)	Normalized ionic current at 1.5 V vs. RHE ($mA\ bar^{-1}\ F^{-1}$)	Normalized ionic current at 1.5 V vs. RHE ($mA\ bar^{-1}\ O\text{-}wt\%^{-1}$)
Vulcan	15	0.36	22.2	36.8	9.7
CNF	4	0.09	2.4	15.5	0.5
CNC	16	0.17	5.0	7.6	0.5
OMC	24	0.38	32.4	34.0	2.9

Interestingly, redox couples associated with the formation/reduction of metal surface oxides (which appear in this potential window as shown in [66]) were not observed on CNFs and CNCs, confirming that the purification treatment with HNO_3 was effective for removing metal impurities from the surface. In fact, the total metal content obtained from ICP was below 1 wt% (see Table S3). In addition, Ni, Cu or Co impurities were not detected by XPS confirming that the surface amount was negligible. Therefore, the residual metal load seems to be encapsulated in the carbon matrixes and it is not accessible for the electrochemical reactions.

3.2.2 Carbon electrooxidation: CO_2 evolution

The anodic faradaic currents observed in the voltammograms of the NCMs (Figure 2, in the potential region from 1.3 to 1.6 V) could be associated with the oxygen evolution reaction (EOR) by water oxidation and/or the CO_2 evolution by carbon corrosion. OER is a key reaction in the air electrode of some batteries and electrolyzers, while carbon corrosion is considered to be one of the main problems facing the performance of fuel cells. Although the electrochemical oxidation of carbon-based electrodes has been widely studied [7, 29, 67], few works have used

spectroelectrochemical techniques [16, 18, 19, 68], which could provide a robust strategy to design effective/stable catalysts.

In this work the performance of nanostructured carbon catalysts in the base electrolyte from -0.1 to 1.6 V was monitored by on line mass spectrometry following the mass signals associated to the formation of O_2 (m/z = 32) and CO_2 (m/z = 44) evolution reactions. The mass signal m/z = 32 did not present changes during the anodic scan showing that oxygen evolution does not take place on carbons at these potentials, and hence, the anodic faradaic currents (from 1.3 to 1.6 V) are only due to carbon oxidation.

Figure 3 shows a comparison of the CVs (upper panel) and the corresponding mass spectrometric cyclic voltammograms (MSCVs) for CO_2 evolution (m/z = 44) of the samples at 5 mV s^{-1} in 0.1 M $NaHCO_3$. First of all, it has to be noted that the GC used as substrate does not contribute significantly to the total faradaic and ionic (m/z = 44) currents of the NCMs. As was expected, a decrease in the graphitic character of the materials led to an increase of the CO_2 formation by corrosion following the sequence: CNFs < CNCs < Vulcan < OMCs. This behavior is explained by differences in the surface heterogeneity of the samples, and consequently, in the amount of surface defects, as well as the surface area. On one hand, it is well known that the higher the surface area the larger the amount of available labile carbon surface sites for carbon oxidation. On the other hand, normalizing the ionic current (m/z = 44) by the capacitance gives an indication of the carbon oxidation rate per unit of electrochemically accessible surface area (Table 4), following the order CNCs < CNFs < OMCs < Vulcan. Surface defects exhibit a higher activity for the adsorption of oxygenated species, which may act as corrosion intermediates [68, 69]. Graphitic materials (CNCs, CNFs) present reduced surface heterogeneity and low density of

surface defects, while non crystalline carbons (Vulcan, OMCs) develop a higher density of active sites [68, 69]. Therefore, derived from a large surface area and a surface more prone to oxidation due to its amorphous character, OMCs displayed the greatest oxidation rate (A g^{-1}). In fact, this material presents the onset potential for CO_2 evolution at 1.0 V vs RHE and the intensity of the mass signal m/z = 44 is several times higher in comparison to those obtained on graphitic carbons (CNCs and CNFs). A significant difference was also found in terms of oxygen speciation and CO_2 evolution rate. Upon normalization of the ionic current (m/z = 44) per surface oxygen content obtained by XPS (Table 4, O_{XPS}) the samples characterized by a high graphitization degree show the lowest normalized ionic current, whereas OMCs and Vulcan, with more labile oxygen groups like carboxylic acids or lactones (Table 3) exhibit larger normalized ionic currents. This corroborates that the presence of more stable oxygen groups, together with low surface area (e.g. CNFs), prevent carbon from electrochemical oxidation.

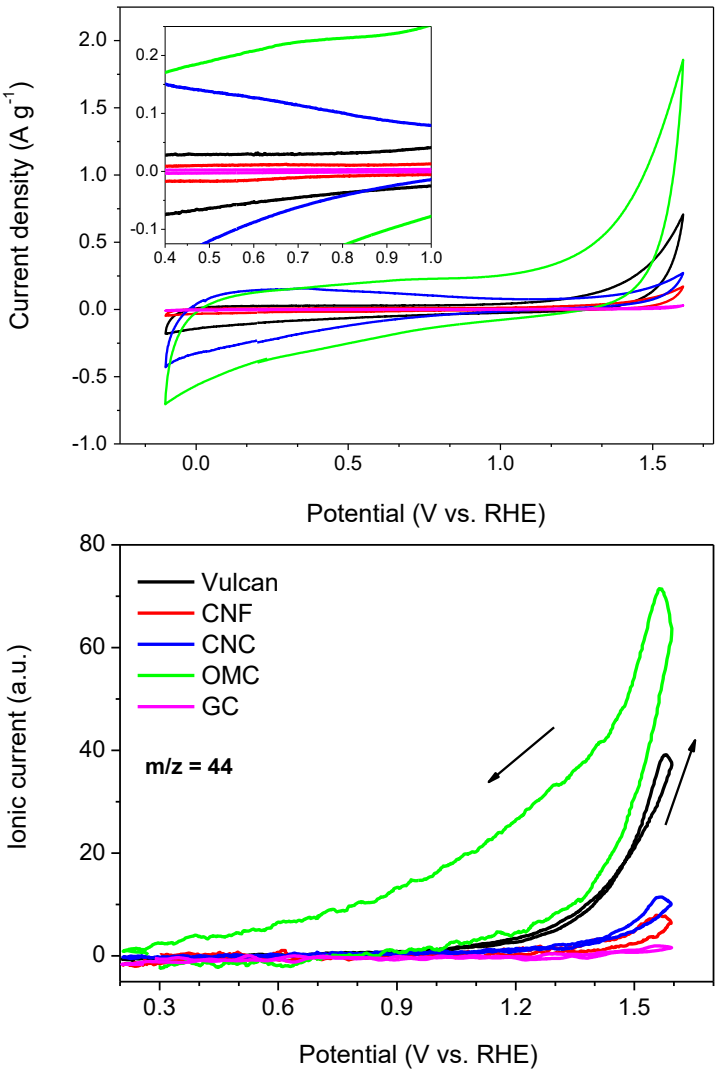

420

421 **Fig. 3.** CVs (upper panel) and MSCVs for CO_2, m/z = 44, (bottom panel) of carbon

422 materials in 0.1 M $NaHCO_3$ (v = 5 mV s^{-1}).

423

424 Subsequently, corrosion tests were carried out cycling 200 times the potential

425 from 0.9 to 1.6 V at 50 mV s^{-1}. CVs were recorded between -0.1 and 1.6 V at 5 mV s^{-1},

426 before and after these experiments to evaluate the influence of surface oxidation on the

427 electrochemical behaviour of NCMs. Simultaneously to the electrochemical analysis,

428 DEMS measurements were performed following the formation of CO_2 (m/z = 44). CVs

429 (upper panel) and MSCVs for m/z = 44 (bottom panel) can be observed in Figure 4,

before (black curves) and after (red curves) potential cycling tests.

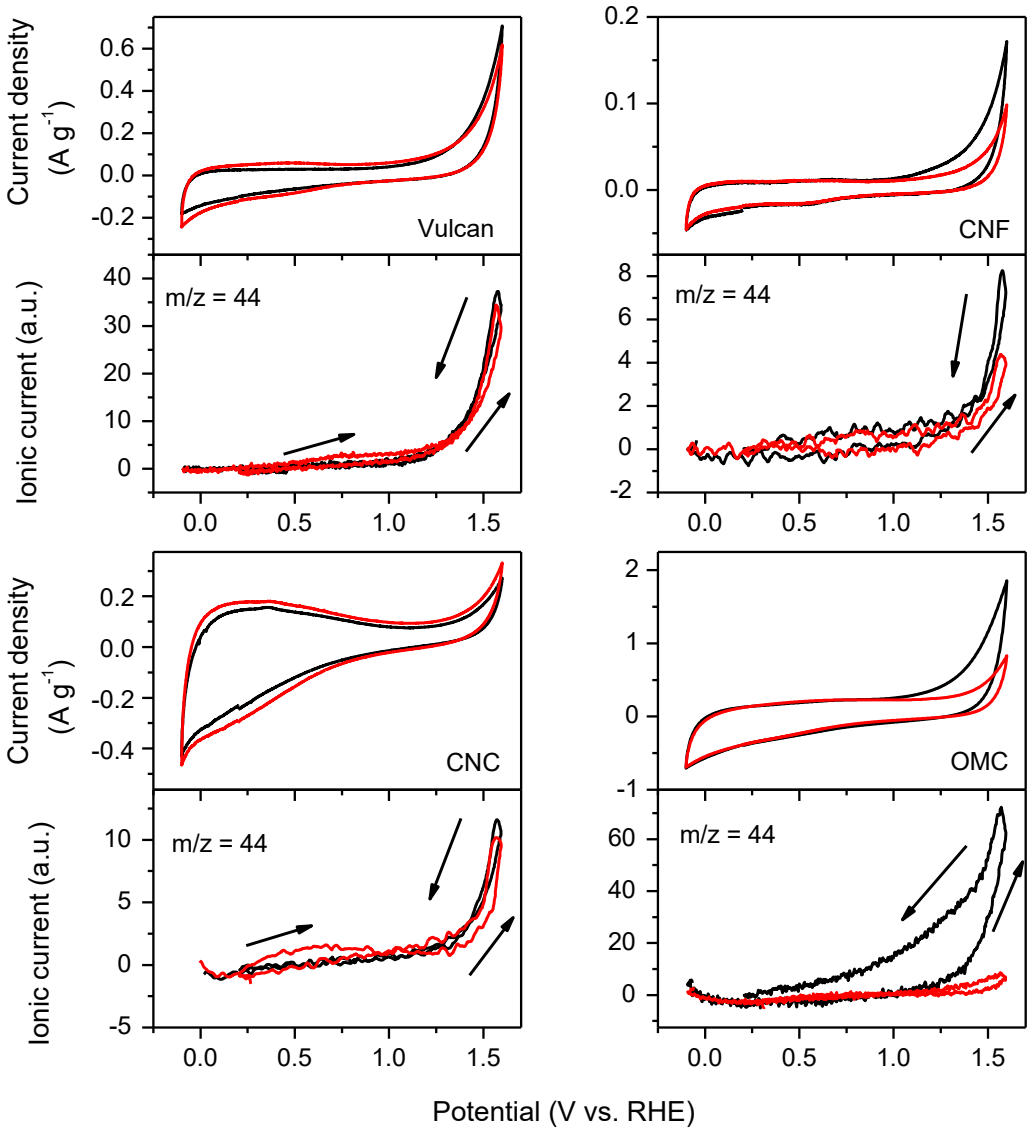

Fig. 4. CVs (upper panels) and MSCVs for CO_2, m/z = 44, (bottom panels) of carbon materials in 0.1 M $NaHCO_3$ (v = 5 mV s^{-1}). Black curves: prior to corrosion tests. Red curves: after 200 cycles at 50 mV s^{-1} between 0.9 and 1.6 V vs. RHE.

Results depend on the nature of the carbon material: CNCs and Vulcan preserved the anodic current and the CO_2 formation at high potentials (1.3-1.6 V), whereas a decrease of both faradaic and ionic (m/z = 44) currents was observed for OMCs and CNFs. Although the origin of this different behaviour is not completely

clear, it can be related to differences in the amount of oxygenated species of the NCMs (Table 2) or in the textural properties (Table 1). According to bibliography [17, 70], a high concentration of adsorbed species on the carbon surface facilitates the gasification of carbon to CO_2 following the Equation 2:

$$C + H_2O \rightarrow CO_2 + 2H^+ + 4e^- \qquad (E^0 = 0.207 \text{ V vs. RHE}) \qquad (2)$$

On the other hand, textural properties play also an important role. A high surface area increases the probability of corrosion. Furthermore, a developed mesoporosity favours the water interaction needed for the formation of oxygenated species, while small pore sizes hinder H_2O diffusion to the active sites. In this context, Vulcan presented a low amount of functional groups and a moderate surface area, and consequently, similar corrosion currents (both faradaic and a CO_2 ionic current) for the first and the 200th cycle were recorded (Figure 4, upper left panel). In contrast, a high content of O atoms nm^{-2} was obtained on CNFs due to the treatment with nitric acid, which may be responsible of the high anodic current related to CO_2 production obtained in the first CV (Figure 4, black curve in upper right panel). In addition, although CNFs exhibited the lowest surface area, they present a significant mesoporosity, which may promote carbon corrosion.

In the case of OMCs, the noticeable current at potentials above 1.3 V in Figure 4 (black curve in bottom right panel) may be attributed to the high surface area of this material and its amorphous character, which enhances carbon corrosion.

Finally, CNCs presented the highest oxygen content but similar corrosion currents during anodic cycling (similar CO_2 production after and before long-term corrosion test) (Figure 4, bottom left panel), which may be explained by their textural features. In fact, CNCs presented similar surface area and mesopore contribution than Vulcan and the same behaviour was obtained for both materials.

Future works will be designed using the identical location transmission electron microscopy with carbon based electrodes to get insights on morphology changes of NCMs upon potential cycling and carbon oxidation.

3.2.3 Catalytic activity towards the HER

At potentials below 0.0 V vs. RHE, the hydrogen evolution reaction (HER) takes place by water reduction in aqueous electrolytes. H_2 evolution is a key reaction in electrochemical energy conversion devices and a lot of works have studied the activity of carbon-supported electrodes [71, 72]. However, the performance of carbon electrodes has not been widely evaluated [32, 37]. In this work, the activity of carbon catalyst based electrodes toward the hydrogen evolution was also evaluated by DEMS. CVs were recorded in the potential range from -0.7 to 1.6 V at 5 mV s^{-1} in the base electrolyte. Simultaneously, the mass signal associated with molecular hydrogen (m/z = 2) was recorded (Figure 5).

It is observed that the HER was favoured in the following order OMC < Vulcan < CNC << CNF. Indeed, a high faradaic current and a large H_2 production (about 15 fold times more than the GC used as substrate) was obtained for CNFs with an onset potential at -0.3 V. Conversely, Vulcan and OMCs presented low H_2 formation (more similar to the GC substrate) in the selected potential range. This improved condition for HER on CNFs and CNCs may be ascribed to their highly graphitic character and/or the presence of metal impurities. It has been reported that delocalized π-electrons of graphene layers act as Lewis bases adsorbing protons from solution and thus aiding the evolution of hydrogen at lower overpotentials [73]. The influence of residual metal impurities, even if below 1wt% according to results from ICP, cannot be discarded even if metal appears encapsulated in the carbonaceous matrixes. Nevertheless, metal traces

were not detected by XPS analyses and the redox couples associated with the formation/reduction of metal oxides were not detected in the CVs for CNFs and CNCs, so the contribution of metal traces to the total current for application in high hydrogen evolution devices (water electrolyzers) is expected to be low even if the turnover frequency is much higher on metals, since the density of metal active sites is much lower than the ones coming from graphene layers in these materials.

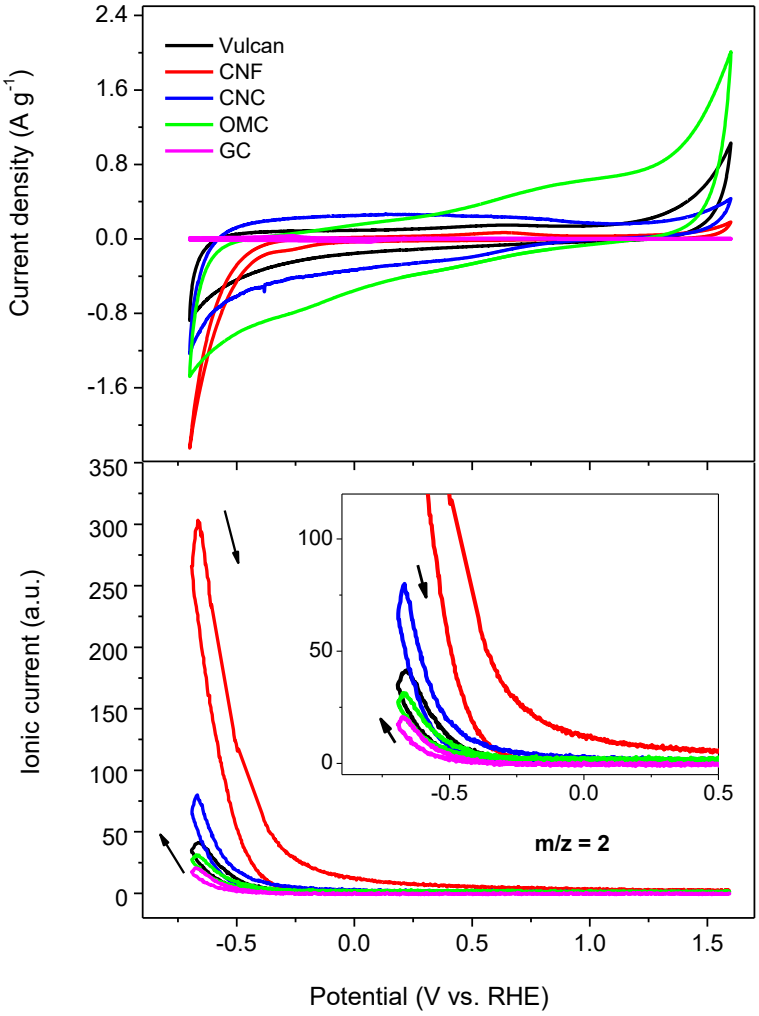

Fig. 5. CVs (upper panel) and MSCVs for H_2, m/z = 2, (bottom panel) of carbon materials in 0.1 M $NaHCO_3$ (v = 5 mV s^{-1}).

It is remarkable that, in the positive-going potential scan, a significant anodic

peak appears in the region from -0.2 to 1.2 V (Figure 5) for all NCMs, which is related to hydrogen oxidation. It can be better observed by comparison of the voltammograms in the potential region from -0.7 to 1.6 V and the blanks (see Figure S4). The high overvoltage required for hydrogen oxidation suggests that hydrogen formed during the cathodic excursion may penetrate inside the porous structure of the carbon bulk and be retained (absorbed hydrogen) or be adsorbed. Then, during the anodic scan, this hydrogen will be oxidized to protons. Several authors have obtained similar results [39, 74-76].

In order to study in detail the hydrogen absorption/adsorption capacity of the NCMs, several CVs were recorded at 5 mV s^{-1} in the base electrolyte, with a stepwise (-0.2 V) shift of cut-off potential to more negative values down to -1.1 V. The obtained curves are given in Figure 6. During the first cycling with the cut-off potential at -0.1 V, only a typical charging of the double layer takes place for all the carbons. At potentials below -0.5 V, the hydrogen absorption/adsorption and its posterior oxidation start to be evident for all the samples. All the NCMs displayed higher currents for hydrogen oxidation while shifting the cut-off potential to more negative values (see graphic insets in Figure 6). However, differences in the potential location of the hydrogen oxidation region were obtained.

Vulcan and OMCs showed a more and more pronounced hump shift toward the positive direction by cycling to more negative potentials. These results prove that hydrogen adsorbs at these catalysts and this adsorption is stronger (at more energetic sites) as the potential is shifted negatively. Consequently, the hydrogen oxidation gradually requires a higher polarization [39, 74-76].

In contrast, the oxidation hump was set at a constant value for CNFs and CNCs, although it is not as evident for the last material due to its wide and not defined

526 hydrogen oxidation region. Considering the CVs in Figure 6, very high currents for
527 HER were found on these carbons at potentials below -0.7 V, showing that the main
528 contribution is hydrogen formation. As a consequence, it is concluded that hydrogen is
529 retained in these samples but the adsorption of hydrogen on high energy places does not
530 proceed. Therefore, the oxidation of absorbed hydrogen is observed but no shift to more
531 positive potentials is recorded. Other authors have obtained a low hydrogen-adsorption
532 capacity on oxidized samples [74, 77].

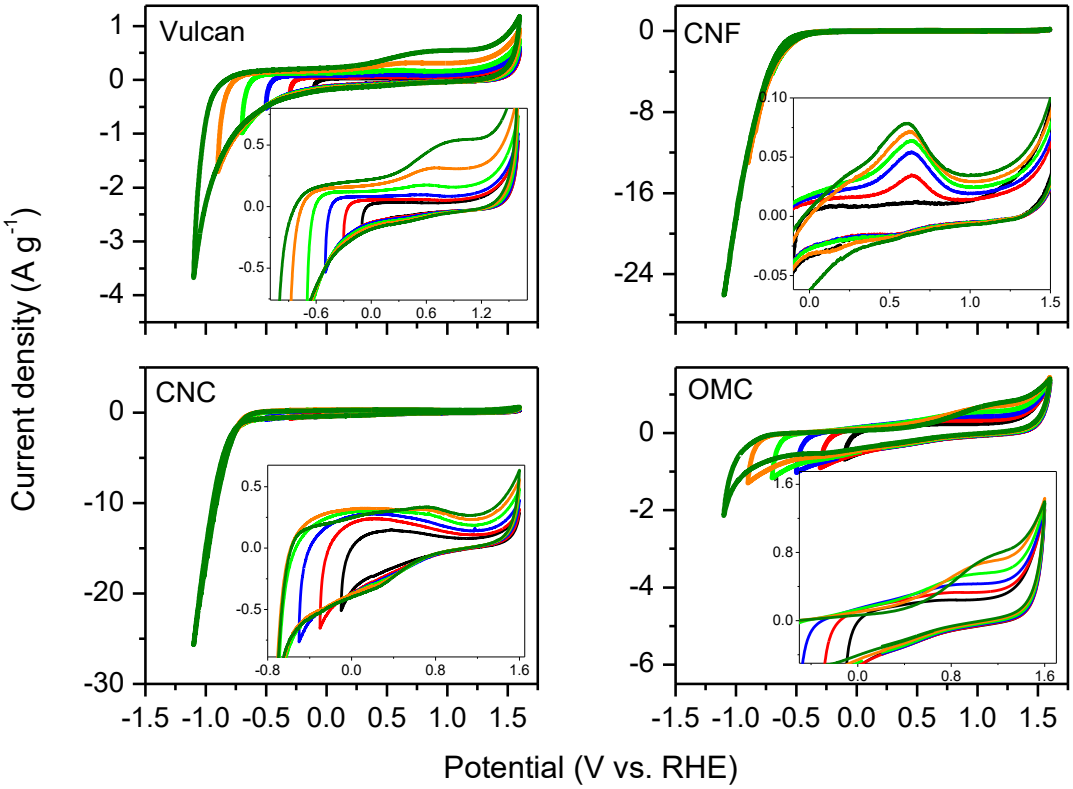

533

534 **Fig. 6.** Dependence of the voltammetry properties of carbon materials in 0.1 M
535 $NaHCO_3$ with the value of negative potential cut-off (v = 5 mV s^{-1}, stepwise = 200 mV).

536

537

538 It is important to note that the oxidation of hydrogen (hump observed at 0.65 for
539 CNFs and 0.74 V for CNCs during the anodic scan) overlaps with the current attributed

to the quinone/hydroquinone groups (created during the metal remove treatments with nitric acid) [76]. Similarly, these carbons displayed a reduction peak during the cathodic scans, at 0.5 V and 0.3 V, respectively.

3.2.4 HER in the presence of CO_2 in the solution: evidences for CO_2 electroreduction

During CO_2 conversion in aqueous electrolytes, the HER occurs as a competitive reaction by the water reduction. However, the presence of adsorbed hydrogen onto the catalyst surface is a requirement for CO_2 activation. Thus, an effective electrode for CO_2 reduction must suppress the HER so that all the adsorbed hydrogen will be consumed only by CO_2 hydrogenation. Recently, high electrocatalytic activities to hydrocarbons and oxygenates have been reported on carbon electrodes [33-36]. However, to the best of our knowledge, this is the first work reporting the electrochemical activity for CO_2 reduction of nanostructured carbons by on-line electrochemical mass spectrometry.

In this work, DEMS experiments were recorded from -1.4 to 0.9 V vs. Ag/AgCl, with the purpose of studying the electrochemical behavior of the nanostructured carbons toward the CO_2 reduction in parallel to the HER. In order to consider the differences of pH between the electrolytes (8.4 in the electrolyte saturated with N_2 and 6.8 after CO_2 saturation), voltammograms were represented versus the RHE using the Equation 3:

$$E_{RHE} = E_{Ag/AgCl} + 0.21 + 0.059\ pH \quad (3)$$

Figure 7 shows the CVs (upper panel) and the corresponding MSCVs for hydrogen evolution (bottom panel) registered at 5 mV s^{-1} in the base electrolyte, in absence (black curves) or in presence (red curves) of dissolved CO_2.

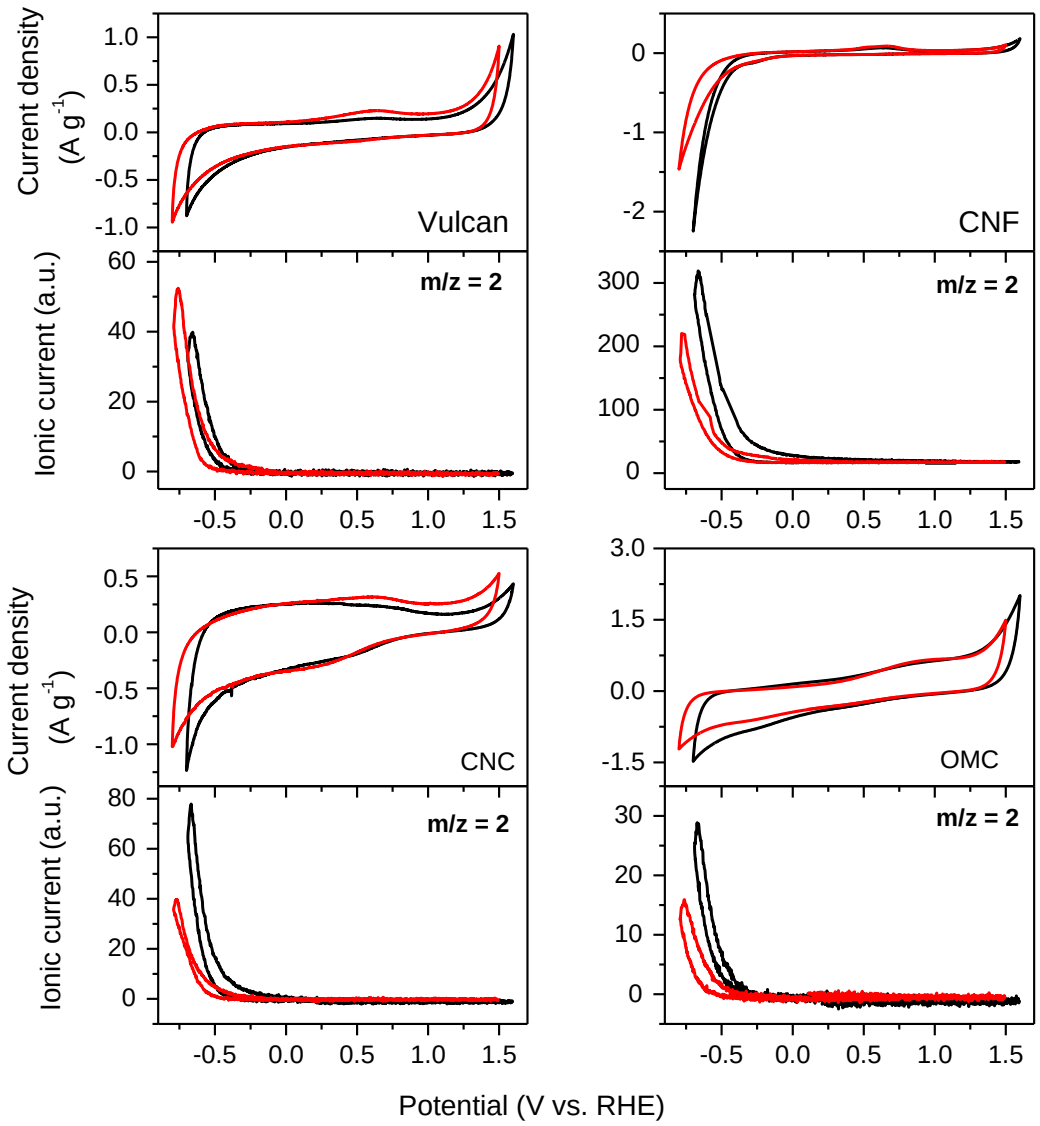

563

564 **Fig. 7.** CVs (upper panels) and MSCVs for H_2, m/z = 2, (bottom panels) of carbon
565 materials in 0.1 M $NaHCO_3$ (v = 5 mV s^{-1}). Black curves: Ar saturated solution. Red
566 curves: CO_2 saturated solution.

567

568 In the presence of CO_2, there is a clear shift of the potential for hydrogen
569 evolution towards more negative values (between 90 and 150 mV negative shift) for all
570 the nanocarbon catalysts. The evidences are clear in terms of both faradaic and ionic
571 (m/z = 2, H_2) currents. This shift might be ascribed to the adsorption of reduced CO_2-
572 related species ($CO_{2,red}$) on the surface of carbon catalysts hindering the adsorption of

hydrogen to the catalytic active sites, and therefore, leading to lower hydrogen evolution rates. Among them, the largest decrease of hydrogen evolution rate was observed for the CNF catalyst, with about 50 % lower faradaic and ionic current density. The extent of diminution in HER rate in the presence of CO_2 can be related to the favorable adsorption of ($CO_{2,red}$) species on the surface of catalytic active sites. This can be interpreted as CNF presenting the highest density of ($CO_{2,red}$) adsorption sites among all the NCMs herein investigated.

According to the bibliography [24, 78, 79], these adsorbates may be mainly $CO_{ad,}$ although the formation of other adsorbed species (such as formates) cannot be discarded. To better identify the possible formation of CO_2 reduction intermediates, current transients stepping the potential from 0.2 to -0.7 V vs. RHE were performed in the CO_2 saturated electrolyte monitoring the mass signals *m/z* =15 (CH_3^+: methane), 30 ($CH_3CH_3^+$ or H_2CO^+: ethane or formaldehyde), 29 ($CH_3CH_2^+$ or CHO^+: ethane/ethanol or an aldehyde), and 45 ($HCHOO^+$ or CH_3CHOH^+: formic acid or ethanol). The formation of electrolysis products was not detected by DEMS indicating that volatile species were not formed at these potentials. As a consequence, the decrease of HER rate might be ascribed to the reversible adsorption of ($CO_{2,red}$) species on the surface of carbon but not following the formation of volatile short-chain organic molecules in this potential window.

CVs at more negative potentials were carried out for the NCMs from -1.8 V to 0.3 V vs. Ag/AgCl (from -1.1 V to 1 V vs. RHE in the case of the electrolyte saturated with Ar and from -1.2 V to 0.9 V vs. RHE in the presence of CO_2) to further research the activity of carbons for CO_2 reduction. The curves in the presence (red curves) and in the absence of dissolved CO_2 (black curves) for each sample are shown in Figure 8. After saturation with CO_2, lower hydrogen evolution cathodic currents were developed

for all carbon materials at -1.1 V vs. RHE that those obtained in the CO_2-free solution corroborating the adsorption of species derived from CO_2 reduction.

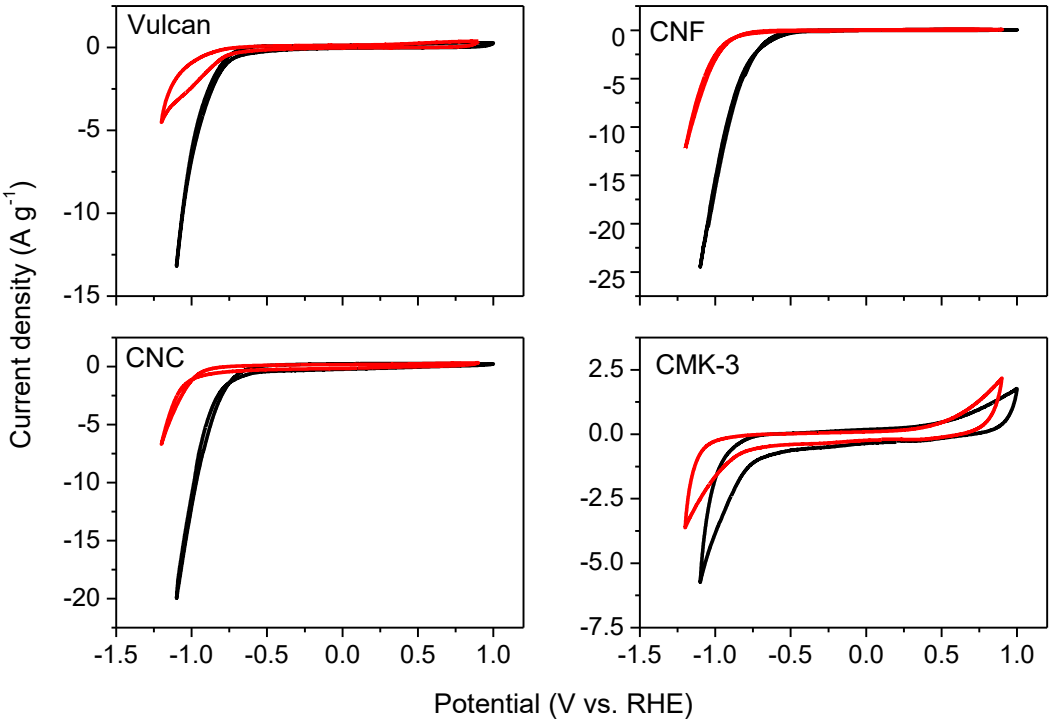

Fig. 8. CVs of carbon materials in 0.1 M $NaHCO_3$ (v = 5 mV s^{-1}) in presence and absence of CO_2. Black curves: Ar saturated solution (from -1.1 V to 1 V vs. RHE). Red curves: CO_2 saturated solution (from -1.2 V to 0.9 V vs. RHE).

Comparing the faradaic current at -1.1 V in the presence and in the absence of CO_2 (black and red curves in Figure 8), a strong inhibition of the current was obtained on the carbon black Vulcan (76%), CNFs (70%) and CNCs (83%), while a lower value was obtained on OMCs (56%), which could be associated to a lower adsorption of ($CO_{2,red}$) intermediates on the last carbon surface. In this context, OMCs exhibited a low cathodic current in absence of CO_2 (see Figure 8, black curve) and consequently, a low hydrogen coverage, resulting in a poor affinity for the adsorption of $(CO_2)_{red}$ species. Moreover, it is well established that the depletion of hydrogen ions in the near surface

of the electrode/electrolyte influences the catalytic behavior [80-82], which effect on the hydrogen evolution is thus more evident for CNF and CNC. These samples are characterized by the highest values of HER rate both in the base and the CO_2-saturated electrolyte.

Finally, significant differences were observed in the HER currents depending on the positive potential limit. On one hand, in the case of the amorphous NCMs (OMCs, Vulcan), when they are cycled up to 1.6 V vs. RHE (Figure 6) the hydrogen evolution current is noticeably lower than when the upper potential is 1.0 V vs. RHE (Figure 8, black curves). More specifically, the current density at -1.1 V vs. RHE decreases from 13.3 A g^{-1} to 3.7 A g^{-1} for Vulcan (72%) and from 5.8 A g^{-1} to 2.1 A g^{-1} for OMCs (64%) when cycling up to 1.6 V vs. RHE. The amorphous nature of carbon together with the narrower porosity of these NCMs lead to the accumulation of oxygenated species during the electrochemical oxidation at highly positive potentials, which results in a decrease of the number of available active sites for HER. Whereas, in the case of CNFs and CNCs there is a slight increase of current (~10%) when cycling up to 1.6 V vs. RHE. Being less prone to corrosion, the catalytically active sites for HER in graphitic carbons are not affected negatively upon applying highly positive potentials but appear to be slightly more active or new active sites are created. Insights on this phenomena will be studied by investigated the morphology of carbon materials by identical location TEM analyses in the future.

4. Conclusions

In this work, the electrochemical and electrocatalytical performances of nanostructured carbon electrodes (CNFs, CNCs, OMCs, Vulcan XC-72R) has been studied by on-line differential electrochemical mass spectrometry (DEMS) in moderate

alkaline media (0.1 M $NaHCO_3$). The capacitance of the different materials is directly related to their surface area and hydrophilicity, as derived from the chemical characterization. DEMS results showed that the faradaic current in the base electrolyte from 1.3 to 1.6 V vs. RHE were associated only with the CO_2 formation (m/z = 44) by carbon corrosion and not with oxygen evolution (m/z = 32). Additionally, it was found that an increase of the graphitic character of the carbons resulted in a decrease of CO_2 generation due to the lower amount of surface defects in graphitic carbons.

On the other hand, spectro-electrochemical measurements showed a different activity toward the H_2 evolution reaction (m/z =2), being the reaction favored on the most graphitic carbon (CNFs) with an ionic current for m/z =2 signal 15 fold times higher than the GC used as substrate.

Finally, H_2 evolution reaction was studied in the presence of CO_2 for evaluation of the materials in the electrochemical reduction of CO_2. A significant decrease in the cathodic current developed in the H_2 evolution region (from -0.5 to -1.1 V vs. RHE) was obtained in a CO_2-saturated 0.1 M $NaHCO_3$ solution for all carbon materials, which demonstrates the adsorption of species derived from CO_2 reduction at all carbon surfaces. However, volatile organic products were not detected by DEMS.

Acknowledgments

The authors gratefully acknowledge financial support given by Spanish MINECO (*CTQ2011-28913-C02-01 and 02*). S. Pérez-Rodríguez acknowledges Gobierno de Aragón for the DGA grant. Furthermore, the authors wish to thank Dra. Ana Beatriz García (INCAR-CSIC) for the TPD measurements.

References

[1] E. Antolini, Appl. Cat. B, 123–124 (2012) 52-68.

[2] A. Walcarius, Chem. Soc. Rev., 42 (2013) 4098-4140.

[3] S. Sharma, B.G. Pollet, J. Power Sources, 208 (2012) 96-119.

[4] C.W.B. Bezerra, L. Zhang, H. Liu, K. Lee, A.L.B. Marques, E.P. Marques, H. Wang, J. Zhang, J. Power Sources, 173 (2007) 891-908.

[5] J. Qiao, Y. Liu, F. Hong, J. Zhang, Chem. Soc. Rev., 43 (2014) 631-675.

[6] J. Zhang, Z. Zhao, Z. Xia, L. Dai, Nat. Nano., 10 (2015) 444-452.

[7] Y. Cheng, S.P. Jiang, Prog. Nat. Sci.: Mater. Int., 25 (2015) 545-553.

[8] S. Tang, G. Sun, J. Qi, S. Sun, J. Guo, Q. Xin, G.M. Haarberg, Chin. J. Catal., 31 (2010) 12-17.

[9] P. Serp, M. Corrias, P. Kalck, Appl. Catal., A, 253 (2003) 337-358.

[10] X. Guo, Y. Zhang, C. Deng, X. Li, Y. Xue, Y.-M. Yan, K. Sun, Chem. Commun., 51 (2015) 1345-1348.

[11] D. Sebastián, I. Suelves, R. Moliner, M.J. Lázaro, A. Stassi, V. Baglio, A.S. Aricò, Appl. Cat. B, 132-133 (2013) 22-27.

[12] T. Hyeon, S. Han, Y.-E. Sung, K.-W. Park, Y.-W. Kim, Angew. Chem. Int. Edi., 42 (2003) 4352-4356.

[13] M.J. Lázaro, V. Celorrio, L. Calvillo, E. Pastor, R. Moliner, J. Power Sources, 196 (2011) 4236-4241.

[14] B. Liu, S. Creager, J. Power Sources, 195 (2010) 1812-1820.

[15] C. Alegre, L. Calvillo, R. Moliner, J.A. González-Expósito, O. Guillén-Villafuerte, M.V.M. Huerta, E. Pastor, M.J. Lázaro, J. Power Sources, 196 (2011) 4226-4235.

[16] S.J. Ashton, M. Arenz, J. Power Sources, 217 (2012) 392-399.

[17] L.C. Colmenares, A. Wurth, Z. Jusys, R.J. Behm, J. Power Sources, 190 (2009) 14-24.

[18] C.-C. Hung, P.-Y. Lim, J.-R. Chen, H.C. Shih, J. Power Sources, 196 (2011) 140-146.

[19] W. Li, A.M. Lane, Electrochem. Commun., 11 (2009) 1187-1190.

[20] Y. Shao, J. Wang, R. Kou, M. Engelhard, J. Liu, Y. Wang, Y. Lin, Electrochim. Acta, 54 (2009) 3109-3114.

693 [21] S. Pérez-Rodríguez, G. García, L. Calvillo, V. Celorrio, E. Pastor, M.J. Lázaro, Int.
694 J. Electrochem., 2011 (2011).

695 [22] S. Pérez-Rodríguez, N. Rillo, M.J. Lázaro, E. Pastor, Appl. Cat. B, 163 (2015) 83-
696 95.

697 [23] G. Centi, S. Perathoner, G. Winè, M. Gangeri, Green Chem., 9 (2007) 671-678.

698 [24] N. Yang, S.R. Waldvogel, X. Jiang, ACS Appl. Mater. Interfaces, 8 (2016) 28357-
699 28371.

700 [25] S. Pérez-Rodríguez, E. Pastor, M.J. Lázaro, J. CO_2 Util., 18 (2017) 41-52.

701 [26] C. Genovese, C. Ampelli, S. Perathoner, G. Centi, J. Energy Chem., 22 (2013) 202-
702 213.

703 [27] M. Gangeri, S. Perathoner, S. Caudo, G. Centi, J. Amadou, D. Bégin, C. Pham-
704 Huu, M.J. Ledoux, J.P. Tessonnier, D.S. Su, R. Schlögl, Catal. Today, 143 (2009) 57-
705 63.

706 [28] O.A. Baturina, Q. Lu, M.A. Padilla, L. Xin, W. Li, A. Serov, K. Artyushkova, P.
707 Atanassov, F. Xu, A. Epshteyn, T. Brintlinger, M. Schuette, G.E. Collins, ACS Catal., 4
708 (2014) 3682-3695.

709 [29] J. Zhang, Z. Xia, L. Dai, Sci. Adv., 1 (2015).

710 [30] N. Cheng, Q. Liu, J. Tian, Y. Xue, A.M. Asiri, H. Jiang, Y. He, X. Sun, Chem.
711 Commun., 51 (2015) 1616-1619.

712 [31] H.B. Yang, J. Miao, S.-F. Hung, J. Chen, H.B. Tao, X. Wang, L. Zhang, R. Chen,
713 J. Gao, H.M. Chen, L. Dai, B. Liu, Sci. Adv., 2 (2016).

714 [32] G. Gao, Y. Jiao, F. Ma, Y. Jiao, E. Waclawik, A. Du, J. Catal., 332 (2015) 149-
715 155.

716 [33] X. Mao, T.A. Hatton, Ind. Eng. Chem. Res., 54 (2015) 4033-4042.

717 [34] W. Li, M. Seredych, E. Rodríguez-Castellón, T.J. Bandosz, ChemSusChem, 9
718 (2016) 606-616.

719 [35] X. Sun, X. Kang, Q. Zhu, J. Ma, G. Yang, Z. Liu, B. Han, Chem. Sci., 7 (2016)
720 2883-2887.

721 [36] J. Wu, S. Ma, J. Sun, J.I. Gold, C. Tiwary, B. Kim, L. Zhu, N. Chopra, I.N. Odeh,
722 R. Vajtai, A.Z. Yu, R. Luo, J. Lou, G. Ding, P.J.A. Kenis, P.M. Ajayan, Nat. Commun.,
723 7 (2016) 13869.

724 [37] G.-f. Long, K. Wan, M.-y. Liu, Z.-x. Liang, J.-h. Piao, P. Tsiakaras, J. Catal., 348
725 (2017) 151-159.

726 [38] Y. Shao, G. Yin, J. Zhang, Y. Gao, Electrochim. Acta, 51 (2006) 5853-5857.

[39] C. Vix-Guterl, E. Frackowiak, K. Jurewicz, M. Friebe, J. Parmentier, F. Béguin, Carbon, 43 (2005) 1293-1302.

[40] K. Jurewicz, C. Vix-Guterl, E. Frackowiak, S. Saadallah, M. Reda, J. Parmentier, J. Patarin, F. Béguin, J. Phys. Chem. Solids, 65 (2004) 287-293.

[41] E. Antolini, Appl. Cat. B, 88 (2009) 1-24.

[42] M. Carmo, V.A. Paganin, J.M. Rosolen, E.R. Gonzalez, J. Power Sources, 142 (2005) 169-176.

[43] S. Pérez-Rodríguez, M. Corengia, G. García, C.F. Zinola, M.J. Lázaro, E. Pastor, Int. J. Hydrogen Energy, 37 (2012) 7141-7151.

[44] S.J. Ashton, M. Arenz, Electrochem. Commun., 13 (2011) 1473-1475.

[45] M.J. Lázaro, L. Calvillo, E.G. Bordejé, R. Moliner, R. Juan, C.R. Ruiz, Microporous Mesoporous Mater., 103 (2007) 158-165.

[46] V. Celorrio, L. Calvillo, S. Pérez-Rodríguez, M.J. Lázaro, R. Moliner, Microporous Mesoporous Mater., 142 (2011) 55-61.

[47] D. Sebastián, I. Suelves, R. Moliner, M.J. Lázaro, Carbon, 48 (2010) 4421-4431.

[48] L. Calvillo, M.J. Lázaro, I. Suelves, Y. Echegoyen, E. García-Bordejé, R. Moliner, J. Nanosci. Nanotechnol., 9 (2009) 4164-4169.

[49] J.L. Figueiredo, M.F.R. Pereira, M.M.A. Freitas, J.J.M. Órfão, Carbon, 37 (1999) 1379-1389.

[50] J.L. Figueiredo, M.F.R. Pereira, M.M.A. Freitas, J.J.M. Órfão, Ind. Eng. Chem. Res., 46 (2007) 4110-4115.

[51] O. Guillén-Villafuerte, G. García, M.C. Arévalo, J.L. Rodríguez, E. Pastor, Electrochem. Commun., 63 (2016) 48-51.

[52] D. Sebastián, A.G. Ruíz, I. Suelves, R. Moliner, M.J. Lázaro, V. Baglio, A. Stassi, A.S. Aricò, Appl. Cat. B, 115 (2012) 269-275.

[53] A. Grondein, D. Bélanger, Carbon, 50 (2012) 4335-4342.

[54] A. Grondein, D. Bélanger, Fuel, 90 (2011) 2684-2693.

[55] H. Chhina, S. Campbell, O. Kesler, J. Power Sources, 179 (2008) 50-59.

[56] D. Banham, F. Feng, T. Fürstenhaupt, K. Pei, S. Ye, V. Birss, J. Power Sources, 196 (2011) 5438-5445.

[57] S. Xiao, S. Liu, J. Zhang, Y. Wang, J. Power Sources, 293 (2015) 119-126.

[58] D. Shao, D. Tang, J. Yang, Y. Li, L. Zhang, J. Power Sources, 297 (2015) 344-350.

[59] H.P. Boehm, Carbon, 40 (2002) 145-149.

[60] A.E. Aksoylu, M. Madalena, A. Freitas, M.F.R. Pereira, J.L. Figueiredo, Carbon, 39 (2001) 175-185.

[61] E. Frackowiak, F. Béguin, Carbon, 40 (2002) 1775-1787.

[62] E. Frackowiak, K. Jurewicz, K. Szostak, S. Delpeux, F. Béguin, Fuel Process. Technol., 77–78 (2002) 213-219.

[63] E. Frackowiak, F. Béguin, Carbon, 39 (2001) 937-950.

[64] R. Mysyk, E. Raymundo-Piñero, F. Béguin, Electrochem. Commun., 11 (2009) 554-556.

[65] L. Wei, G. Yushin, Nano Energy, 1 (2012) 552-565.

[66] S. Gao, X. Jiao, Z. Sun, W. Zhang, Y. Sun, C. Wang, Q. Hu, X. Zu, F. Yang, S. Yang, L. Liang, J. Wu, Y. Xie, Angew. Chem. Int. Ed., 55 (2016) 698-702.

[67] N.-T. Suen, S.-F. Hung, Q. Quan, N. Zhang, Y.-J. Xu, H.M. Chen, Chem. Soc. Rev., 46 (2017) 337-365.

[68] S. Maass, F. Finsterwalder, G. Frank, R. Hartmann, C. Merten, J. Power Sources, 176 (2008) 444-451.

[69] B. Avasarala, R. Moore, P. Haldar, Electrochim. Acta, 55 (2010) 4765-4771.

[70] H.-S. Oh, K. Kim, Y.-J. Ko, H. Kim, Int. J. Hydrogen Energy, 35 (2010) 701-708.

[71] F. Safizadeh, E. Ghali, G. Houlachi, Int. J. Hydrogen Energy, 40 (2015) 256-274.

[72] P.C.K. Vesborg, B. Seger, I. Chorkendorff, J. Phys. Chem. Lett., 6 (2015) 951-957.

[73] M.S. Shafeeyan, W.M.A.W. Daud, A. Houshmand, A. Shamiri, J. Anal. Appl. Pyrolysis, 89 (2010) 143-151.

[74] K. Fic, E. Frackowiak, F. Beguin, J. Mater. Chem., 22 (2012) 24213-24223.

[75] F. Béguin, K. Kierzek, M. Friebe, A. Jankowska, J. Machnikowski, K. Jurewicz, E. Frackowiak, Electrochim. Acta, 51 (2006) 2161-2167.

[76] K. Jurewicz, E. Frackowiak, F. Béguin, Appl. Phys. A, 78 (2004) 981-987.

[77] M.J. Bleda-Martínez, J.M. Pérez, A. Linares-Solano, E. Morallón, D. Cazorla-Amorós, Carbon, 46 (2008) 1053-1059.

[78] P.A. Christensen, A. Hamnett, A.V.G. Muir, N.A. Freeman, J. Electroanal. Chem., 288 (1990) 197-215.

[79] K. Hara, A. Kudo, T. Sakata, J. Electroanal. Chem., 421 (1997) 1-4.

[80] M. Auinger, I. Katsounaros, J.C. Meier, S.O. Klemm, P.U. Biedermann, A.A. Topalov, M. Rohwerder, K.J.J. Mayrhofer, Phys. Chem. Chem. Phys., 13 (2011) 16384-16394.

[81] I. Katsounaros, J.C. Meier, S.O. Klemm, A.A. Topalov, P.U. Biedermann, M. Auinger, K.J.J. Mayrhofer, Electrochem. Commun., 13 (2011) 634-637.

[82] D. Strmcnik, M. Uchimura, C. Wang, R. Subbaraman, N. Danilovic, V. van der, A.P. Paulikas, V.R. Stamenkovic, N.M. Markovic, Nat Chem, 5 (2013) 300-306.